

Investigating the role of ocean-atmosphere coupling in the North Pacific Ocean

DIMITRY SMIRNOV ^{*} AND MATTHEW NEWMAN

CIRES, University of Colorado, and NOAA/Earth System Research Laboratory, Boulder, Colorado

MICHAEL A. ALEXANDER

NOAA/Earth System Research Laboratory, Boulder, Colorado

^{*} *Corresponding author address:* Dmitry Smirnov, NOAA/ESRL, 325 Broadway, R/PSD1, Boulder, CO 80305.
E-mail: dima.smirnov@noaa.gov

ABSTRACT

Air-sea interaction over the North Pacific is diagnosed using a simple, local coupled autoregressive model constructed from observed 7-day running mean sea-surface temperature (SST) and 2-m air temperature (T_A) anomalies during the extended winter from the $1^\circ \times 1^\circ$ OAFlux dataset. Though the model is constructed from one-week lag statistics, it successfully reproduces the observed anomaly evolution through lead times of 90 days, allowing an estimation of the relative roles of coupling and internal atmospheric and oceanic forcing upon North Pacific SSTs. It is found that east of the dateline, SST variability is maintained by, but has little effect on, T_A variability. However, in the Kuroshio-Oyashio confluence and extension region, about half of the SST variability is independent of T_A , driven instead by SST noise forcing internal to the ocean. Including surface zonal winds in the analysis does not alter this conclusion, suggesting T_A adequately represents the atmosphere. Repeating the analysis with the output of two control simulations from a fully-coupled global climate model (GCM) differing only in their ocean resolution yields qualitatively similar results. However, for the simulation employing the coarse-resolution (1°) ocean model, all SST variability depends upon T_A , apparently caused by a near absence of ocean-induced noise forcing. Collectively, these results imply that a strong contribution from internal oceanic forcing drives SST variability in the Kuroshio-Oyashio region, which may be used as a justification for atmospheric GCM experiments forced with SST anomalies in that region alone. This conclusion is unaffected by increasing the dimensionality of the model to allow for intra-basin interaction.

1. Introduction

The importance of air-sea interaction to extratropical atmospheric variability has been the subject of research for over 50 years (Namias 1959; Bjerknes 1964). The fundamental issue is that while sea-surface temperature (SST) anomalies are largely forced by the atmosphere (Cayan 1992), they can feed back onto the atmosphere (Kushnir et al. 2002). This coupled system was expressed simply by Barsugli and Battisti (1998), hereafter BB98, as:

$$\frac{d}{dt} \begin{bmatrix} T_A \\ T_S \end{bmatrix} = \begin{bmatrix} a & b \\ c & d \end{bmatrix} \begin{bmatrix} T_A \\ T_S \end{bmatrix} + \begin{bmatrix} \xi_A \\ 0 \end{bmatrix} \quad \begin{array}{l} b : T_S \rightarrow T_A \\ c : T_A \rightarrow T_S \end{array} \quad (1)$$

where T_S and T_A are anomalous SST and surface air-temperature, respectively, and ξ_A represents random atmospheric forcing (e.g. synoptic weather variability) that exists regardless of SST variability. The diagonal coefficients a and d represent the intrinsic damping of T_A and T_S , respectively, while the off-diagonal elements b and c quantify the coupling: b is the effect of $T_S \rightarrow T_A$, vice versa for c . Equation (1) can be considered a null hypothesis for air-sea coupling and an extension to the simpler null hypothesis of atmospheric forcing of the uncoupled ocean (Frankignoul and Hasselmann 1977; hereafter, FH77). Notably, this hypothesis implies that internal oceanic variability is not important in forcing T_S anomalies.

BB98 suggested that coupling increases the persistence of SST anomalies by $\sim 50\%$ through “reduced thermal damping”; that is, as T_A adjusts to the underlying SST at longer timescales, the heat-flux between the two (in a system driven purely by T_A) tends to zero. Consequently, running long-duration atmospheric global climate models (GCMs) forced in the extratropics by observed historical SST anomalies is problematic due to a large, potentially spurious *upward* surface heat flux (latent + sensible; upward being from the ocean to the atmosphere) at low frequencies (BB98; Saravanan 1998; Bretherton and Battisti 2000; Sutton and Mathieu 2002). In addition, previous large-scale SST-forced AGCM experiments (e.g. Peng et al. 1995, 1997; Kushnir and Held 1996; Kushnir et al. 2002) have not, in general, tended to support a significant role for extratropical SST forcing of the atmosphere. This

is in stark contrast to the well-documented role of tropical SST anomalies in remotely generating extratropical atmospheric and SST anomalies (e.g. Ferranti et al. 1994; Alexander et al. 2002; Hoerling and Kumar 2002).

The assumption made by FH77 and BB98 is that SSTs are driven purely by random atmospheric variability. However, in the vicinity of western boundary currents (WBCs), SST variability is not simply a passive response to surface heat flux forcing (Frankignoul and Reynolds 1983), but instead may be forced by ocean dynamics and transport (Kelly 2004). For example, westward oceanic Rossby wave propagation resulting from anomalous wind stress curl forcing in the central and eastern Pacific (Deser et al. 1999; Schneider et al. 2002) can result in anomalous heat transport within the Kuroshio current that is of the same order of magnitude as the surface heat flux, often changing the sign of the SST tendency implied from the surface heat flux alone (Qiu 2000). Ekman advection, especially in the vicinity of SST fronts, can also be an important factor in driving SST changes as shown for the North Pacific by Miller et al. (1994). In fact, Lee et al. (2008) extended the BB98 model through the inclusion of SST noise (as a function of atmospheric noise) and found that this could substantially mitigate the impact of reduced thermal damping. Dong and Kelly (2004) suggest that Ekman advection plays a secondary role to geostrophic currents in forcing mixed-layer temperature changes within the upper 400-m layer of the Gulf Stream, although since 400-m is substantially deeper than the Ekman layer, they may have underestimated the direct role of Ekman currents on SST.

Additionally, Nakamura et al. (2004) showed that the most active regions of synoptic atmospheric eddies are strongly collocated with WBCs and their associated SST fronts, creating intense upward surface heat fluxes. However, whether this collocation is caused by the strong SST gradient (Minobe et al. 2008) or from the land-sea thermal contrast (Brayshaw et al. 2009, 2011) is still an open question. Regardless, the rapid T_A damping time scales (up to 1 day^{-1} ; Nonaka et al. 2009) over the SST gradient can be expected to be partially due to the differential sensible heat flux forcing maintained by the SST front

(Nakamura et al. 2008; Taguchi et al. 2009). In short, there is evidence that air-sea interaction may exhibit differences within the western portions of extratropical oceans compared to the east due to the elevated role of internal oceanic thermal processes.

The purpose of this study is to examine how air-sea interaction differs across the extratropical North Pacific. We construct an empirical version of the local, coupled model of BB98 (1) from the relatively new OAFlux observational dataset (Yu and Weller 2007). Unlike BB98, however, we allow for the possibility of both T_A and T_S stochastic forcing. There are several questions we seek to answer. Is the local, coupled model equally valid across different portions of the North Pacific? If not, can the model be improved by allowing for non-local interaction? Does the role of coupling have a geographical dependence? How significant is the omission of oceanic noise in BB98’s model? And finally, how well do coupled global climate models (GCMs) capture mid-latitude air-sea interaction within our framework?

The manuscript is ordered in the following manner. In Section 2, we describe the observational and coupled GCM datasets and how the empirical model is constructed. Section 3 contains the main results, including the spatial structure of the coupled model coefficients, and an evaluation of how well the model reproduces observed statistics and how coupling varies across the basin. Also in section 3 is a comparison of how the empirical model performs when applied to the output of a coupled GCM. In Section 4, we consider the role of remote forcing and whether it changes the interpretation of the local model. Finally, conclusions are provided in Section 5, along with open questions stemming from this study.

2. Constructing the local, coupled model

a) Observations

In contrast to BB98, we develop the local, coupled model *empirically* using linear inverse modeling (LIM; Penland 1989; Mosedale et al. 2005). In this case, the LIM portrays a

bivariate Markov process that is forced by Gaussian white noise ξ :

$$\frac{d\mathbf{x}}{dt} = \mathbf{L}\mathbf{x} + \xi \quad (2)$$

where the state vector $\mathbf{x}(t) = [T_A(t) \ T_S(t)]^T$ represents the time evolution of 7-day running mean anomalies of 2-m air temperature (T_A) and SST (T_S) taken from the $1^\circ \times 1^\circ$ OAFflux dataset (Yu and Weller 2007) from 1985-2009. Note that in contrast to BB98, ξ includes both T_A and T_S noise forcing (Zubarev and Demchenko 1992). We focus on the North Pacific (20° - 60° N, 120° - 270° E) during the extended boreal winter months (November-March), which reduces the role of reemergence on T_S anomalies (Alexander and Deser 1995). Repeating the analysis on the winter-only period (December-February) yields very consistent results. To avoid the impact of sea-ice, all grid points where the minimum SST is below -1.8°C are excluded. \mathbf{L} is the feedback, or deterministic, matrix of similar coefficients as in BB98:

$$\mathbf{L} = \begin{bmatrix} a & b \\ c & d \end{bmatrix}.$$

The determination of \mathbf{L} and other details regarding the LIM can be found in the Appendix. Briefly, a LIM is fit to each point [by finding \mathbf{L} using the lagged covariance of \mathbf{x} via (A1) and noise covariance $\mathbf{Q} = \langle \xi \xi^T \rangle dt$ as a residual in the fluctuation-dissipation relation via (A3)]; collectively, we refer to the 1-D (bivariate) model as the local-LIM. Note that we term an “uncoupled” system as one where $b, c = 0$. In contrast, BB98 refer to “uncoupled” where only $b = 0$ since their aim was to contrast a system with a slave-ocean to that with prescribed SST (setting $b, c = 0$ in BB98 would result in no SST variability). Since we do not assume a passive ocean, but instead use observations to determine the amount of oceanic influence through \mathbf{Q} , we are able to also set $c = 0$ to determine the intrinsic role of the ocean.

There are several methods to assess the performance of the LIM. One approach is to determine cross-validated forecast skill where starting with $\mathbf{x}(t)$, one can make predictions

at various lead times via (A2) and compare to the observed evolution (Winkler et al. 2001; Newman et al. 2003; Kossin and Vimont 2007; Pegion and Sardeshmukh 2011). Because the local-LIM has skill comparable to that of the FH77 T_S -only model (not shown), its value is predominantly of diagnostic nature. Instead of assessing forecast skill, we compare the predicted covariance (diagonal elements of $\mathbf{C}(0)$ and $\mathbf{C}(\tau)$, see Appendix) and cross-covariance (off-diagonal elements) to observations as a function of lead time. Nonetheless, we later present skill when comparing the local-LIM with a higher-order LIM that allows for remote interaction (section 4). Finally, while the focus here is mainly on seasonal variability, one must remember that the LIM provides a red-noise null hypothesis on all timescales.

b) Coupled GCMs

Recently, it has been recognized that course-resolution coupled models generally underestimate smaller-scale oceanic features such as mesoscale eddies and mid-latitude SST fronts (Small et al. 2008). For example, Bryan et al. (2010) showed that the ocean component of a coupled GCM must be eddy-resolving in order to reproduce the magnitude of the observed positive correlation between small-scale wind-stress and SST anomalies found in earlier studies (e.g. Chelton et al. 2004; Xie 2004). To investigate air-sea interaction within coupled models, we extend the LIM analysis to two simulations of the Community Climate System Model (CCSM) version 3.5, developed by the National Center for Atmospheric Research (NCAR) (Gent et al. 2010). The simulations only differ in their ocean model, which has a resolution of 0.1° (1°) in the high (low) resolution simulation. Details of these simulations are available in Kirtman et al. (2012) (also Bryan et al. 2010) and hereafter we refer to the high- (low-) resolution simulations as HR (LR). To maintain consistency with the OAFlux-based local-LIM, the output of both GCMs is linearly interpolated to the OAFlux $1^\circ \times 1^\circ$ grid and 25 years of data are sought. However, only 19 years of data are available for the LR simulation. Because a shorter record could affect the fit of \mathbf{L} in (A2), we accessed 30 years of an additional 1° CCSM simulation from the slightly later version 4 (Gent et al. 2011; C.

Hannay, personal communication). Aside from small differences in the mean climate (e.g. position of WBCs), the LIM coefficients and coupling characteristics of both low-resolution simulations appear very comparable and only LR is discussed hereafter.

3. Results

a) Observed and predicted covariance

Figure 1 shows the wintertime standard deviation (σ) of weekly-averaged T_S anomalies (σ_S ; Fig. 1a), and weekly- and daily-averaged T_A anomalies (σ_A ; Fig. 1b,c respectively). Due to the ocean's large thermal inertia, computing σ_S by averaging T_S over increasing timescales (daily to weekly to monthly) has a negligible influence on variance (not shown). Enhanced T_S variability is found within the Kuroshio/Oyashio confluence and separation region immediately east of Japan (Mitsudera et al. 2004), their extensions near 40°N , 170°E (Kwon et al. 2010) and a broad region from the dateline, 30°N , northeast to 40°N , 150°W associated with subtropical front variability (Nakamura et al. 1997) and ENSO teleconnections (Alexander 1992; Diaz et al. 2001). In contrast to T_S , and due to the presence of short-lived synoptic eddies, σ_A is reduced on average by 30% after taking weekly averages (compare Fig. 1b to 1c, note different color scales). However, the reduction is non-uniform as σ_A is reduced by 50% east of Japan but only by 10-20% in the northeastern Pacific. Thus, our use of 7-day running mean anomalies implies that a modest portion of variability is lost in the most active part of the North Pacific storm track. However, the 7-day running mean provides a good compromise between retaining variability and maintaining accurate predictions of lag covariance (see appendix).

The spatial variability of the \mathbf{L} coefficients is shown in Figure 2a-d. A Monte Carlo test using synthetically generated data (see Section 3b for details) suggests that the standard error for coefficients a, c, d is $\sim 10\%$, while that of b is $\sim 20\%$ (likely due to the shortness of the record; see Mosedale et al., 2005). For reference, the coefficients obtained by BB98, $(a, b, c, d) = (-0.22, 0.10, 0.01, -0.01)$, would be most representative of a point in the Gulf

of Alaska. Diagonal coefficients a, d are damping timescales (in days^{-1}), while off-diagonal coefficients b, c represent coupling strength ($b : T_S \rightarrow T_A$; $c : T_A \rightarrow T_S$). Coefficients a and d are negative everywhere, as expected due to the damping of SST and T_A to climatology through radiative and surface heat flux anomalies (BB98; Frankignoul and Kestenare 2002; Park et al. 2005), regardless of coupling. Note that the T_S damping rate d varies by a factor of 3 across the North Pacific, with the smallest values of $|d|$ (i.e. greatest persistence) occurring in regions of strong currents and/or large mixed-layer (ML) depths extending from Japan northeast into the central North Pacific (Alexander 2010). Meanwhile, highest values of $|d|$ (greatest damping) occur in the subtropical regions of shallow ML depths, where even weak atmospheric forcing can quickly modify SST through surface fluxes and wind-forced entrainment of sub-ML water (Frankignoul 1985; Alexander et al. 2000). Note that this mechanism may also explain the large values of the coupling coefficients in the subtropical region. Conversely, values of the off-diagonal elements are everywhere positive, consistent with reduced thermal damping of both T_S and T_A (BB98). We can compare our T_S feedback strength, b , to previous mid-latitude heat flux feedback estimates of 20-30 $\text{W m}^{-2} \text{ } ^\circ\text{C}^{-1}$ (e.g. Frankignoul and Kestenare 2002; Park et al. 2005) by converting b into an energy flux that acts on an atmospheric slab of thickness H_a , density ρ_a and heat capacity C_a . Even when using an 800-mb thick slab ($H_a \approx 12000 \text{ m}$; i.e. supposing the feedback acts on the entire troposphere), $\bar{\rho}_a = 0.80 \text{ kg m}^{-3}$, $C_a = 1000 \text{ J kg}^{-1} \text{ } ^\circ\text{C}^{-1}$ and the median value of $b = 0.11(^{\circ}\text{T}_A \text{ } ^\circ\text{T}_S^{-1} \text{ day}^{-1})$, we estimate a feedback strength $\alpha = b\bar{\rho}_a C_a H_a$ of 12 W m^{-2} , which is lower than previous estimates. The discrepancy signals that previous estimates may have convolved the forcing and feedback, though our estimate may be conservative since we do not explicitly account for wind, moisture and stability anomalies.

The usefulness of any model is gauged by its ability to reproduce observations. Figure 3 shows the observed lag-covariance, $\mathbf{C}(\tau)$, for T_S and T_A with $\tau=(30,60,90)$ representing the degree of persistence over the course of those periods. Regions of high T_S persistence coincide with regions of high T_S variability (cf. Fig. 3a,c,e with Fig. 1a) consistent with the

dominance of slow processes in the ocean. T_A persistence generally resembles that of T_S east but not west of the dateline (most notably differing in the WBC region), implying either weaker or non-local coupling there as may be expected due to the rapid T_A variability. Figure 3 also shows where the difference between $\mathbf{C}(\tau)$ and predicted covariance, $\tilde{\mathbf{C}}(\tau)$, significantly differs at the $p = 0.025$ level [based on 200 iterations of a Monte Carlo test where \mathbf{x} is subsampled with replacement during the extended winter months]. For $\tau=30$ days, the LIM predicts $\tilde{\mathbf{C}}(\tau)$ very well; as lead time increases (Fig. 3c-f), the LIM continues to do well west of the dateline, but somewhat underestimates SST persistence east of the dateline, perhaps because remote ENSO forcing (e.g. Alexander et al. 2002) is not fully captured by the local-LIM. For long lags, an additional complication is a changing mixed layer depth, which will clearly affect the coefficients in \mathbf{L} . Meanwhile, Figure 3b,d,e shows that $\tilde{\mathbf{C}}(\tau)$ for T_A displays similar characteristics as T_S , although persistent T_A variability is limited to east of the dateline. The predicted lag cross-covariance (i.e. off-diagonal elements of $\tilde{\mathbf{C}}(\tau)$ when T_S either leads or lags T_A) shows very similar characteristics as Fig. 3 and is discussed further in Section 4.

The local-LIM predicts $\tilde{\mathbf{C}}(\tau)$ for T_S in the WBC region remarkably well despite the concern of previous studies when using the FH77-type model in a dynamically active ocean region (Reynolds 1978; Hall and Manabe 1997). The chief issue is how the local-LIM treats oceanic processes, which are either represented deterministically in the T_S damping coefficient d or are captured by T_S noise forcing. Since the LIM is trained using a 7-day lag, it is possible that d also implicitly includes the effect of anomalous currents and perhaps the aggregate effect of mixing by eddies. This can be further investigated by both increasing the training lag (though with the expense of smoothing the data) and incorporating other variables such as sea-surface height anomalies, but we leave this matter for future research. Frankignoul and Reynolds (1983) extended the FH77 model to include an estimate of the mean current acting on anomalous ∇T_S , finding only a slightly increased T_S persistence time on seasonal timescales. However, they were not able to estimate the role of anomalous

currents and their use of EOF-filtered $5^\circ \times 5^\circ$ data likely suppressed all oceanic eddy activity. To gain some insight into the role of internal oceanic processes in the local-LIM, we chose to investigate the spatial structure and spectrum of the noise forcing.

We approximate the noise forcing ξ of SST (T_A) in (2) as η_S (η_A), a residual from the integration of (2) over a short time period ($\Delta t = 1$ day):

$$\eta(t) = \frac{\mathbf{x}(t + \Delta t) - \mathbf{x}(t)}{\Delta t} - \mathbf{L}\mathbf{x}(t). \quad (3)$$

Figure 4a shows the power spectra of SST, η_A and η_S for 20 randomly sampled points over the North Pacific (shown as dots in Fig. 4c), including five points within the WBC region. Note that η is found after rebuilding the local-LIM using annual data, which has little to no effect on the main findings (i.e. the full-year \mathbf{L} is similar to the wintertime-only \mathbf{L} but allows for the continuous estimation of η). The power of observed SST variance increases rapidly for $\omega < 30$ days $^{-1}$, follows the ω^{-2} curve through $\omega \sim 300$ days $^{-1}$ and begins to asymptote as damping dominates for lower-frequencies (Frankignoul 1985). Meanwhile, the spectra of η_S , while slightly reddened for $\omega > 50$ days $^{-1}$, is nearly flat for lower frequencies implying that the impact of oceanic processes on T_S is adequately approximated as white noise for $\omega < 50$ days $^{-1}$. An F-test (not shown) reveals that the power spectra of η_S does not significantly differ ($p=0.025$) from an AR1 null hypothesis using a relatively short decorrelation timescale of 15 days. Similar conclusions are reached about η_A , except its decorrelation timescale is an even shorter 5 days, which given the use 7-day running mean used for \mathbf{x} can be justified as nearly white noise.

To investigate the extent to which the noise forcing varies across the North Pacific, Fig. 4b,c shows the diagonal elements of \mathbf{Q} , which represent the variances of T_A and T_S noise forcing, respectively. Figure 4c shows that T_S forcing is maximized in the WBC region, which represents the aggregate impact on T_S forcing from anomalous currents, gradients and mesoscale eddy activity portrayed by ξ_S in (2). To directly compare our model to BB98, the fluctuation-dissipation relation is used to find the amount of T_S variance in the absence

of T_S noise forcing (not shown). Not surprisingly, only 20-30% of T_S variance remains within the WBC, while 60-70% is retained in the eastern portion of the North Pacific (the latter number is likely an underestimate since the LIM does not have ENSO-forced T_A variability, see Fig. 3). Meanwhile, even taking into account the 7-day smoothing, the strongest T_A forcing occurs just offshore of the Asian continent and extends over the WBC region (Fig. 4b), associated with the North Pacific storm track variability (Nakamura et al. 2004). Finally, a secondary maximum of T_A noise forcing along the southern coast of Alaska coincides with weak T_S variability (cf. Fig. 1a) there and we do not discuss this further.

b) The role of coupling

In the previous section, it was shown that the local-LIM adequately represents observed extratropical T_A and T_S coupled variability on weekly timescales over the course of a season. As originally suggested in BB98, coupling boosts persistence of both T_A and T_S anomalies. However, the non-homogeneity of the coupling coefficients (cf. Fig. 2 b,c) raises the questions: what are the impacts of the differing coupling strength across the North Pacific? and, how sensitive are the T_A and T_S variances to the coupling strength? We approach this question by determining what the variability would be for a system like (2) with the same noise forcing but with uncoupled dynamics \mathbf{L}^u and noise \mathbf{Q}^u (that is, where \mathbf{L} is modified to remove the effects of coupling by setting $b = c = 0$, and \mathbf{Q} has been modified by setting the off-diagonal elements to 0). We create two synthetic data sets by numerically integrating (2) for 9000 days, with either \mathbf{L} and \mathbf{Q} or \mathbf{L}^u and \mathbf{Q}^u , for each grid point using the numerical method outlined by Penland and Matrosova (1994) and a time step of 2 hours. The integration using \mathbf{L} forced by the observed noise covariance yields coupled T_S and T_A variability that reproduces the observed variance to within 5% (ensuring the numerical method works properly), while integration of (2) with \mathbf{L}^u yields time series of uncoupled variability, T_S^u and T_A^u .

Figure 5 shows the ratio of uncoupled to coupled variance for T_S and T_A (in Fig. 5a, T_S and T_S^u have been monthly averaged before calculating this ratio). Over large areas of

the North Pacific, SST variability is nearly eliminated without coupling, with the notable exception of the WBC region where 40-70% of SST variability is retained. The use of 1° data implies that the results in the latter region may be underestimated (Taguchi et al. 2009), and in the future it may be worthwhile to redo this calculation with higher resolution datasets. A second region with relatively large intrinsic T_S variability is located within and just south of the Bering Sea, which is potentially related to oceanic processes associated with variability in the sea-ice edge and is not discussed further. In contrast to T_S , T_A variability is largely retained after uncoupling (Fig. 5b), confirming that the ocean’s impact on the atmosphere is much weaker than the atmosphere’s impact on SST. A relative minimum in the fraction of uncoupled T_A variability occurs from 20°N , 165°E to about 40°N , 150°W , which is also where b, c are largest (Fig. 2b,c) suggesting this is where local coupling is most important. Meanwhile, nearly all *persistent* T_A variability [represented by $\mathbf{C}(\tau > 14 \text{ days})$ and arising mainly from the feedback by T_S], is eliminated in the absence of coupling (not shown), though note that this is limited to the ENSO teleconnection region east of the dateline (see Fig. 3f). Still, Fig. 5 clearly shows that outside of the WBC region, the atmosphere is the ultimate source of air-sea variability.

One caveat in our treatment of air-sea interaction is the absence of wind-forcing. Since we do not explicitly consider anomalous wind (\mathbf{U} , representing u and v) in the local-LIM, it is possible that T_S anomalies generated via Ekman transport are being erroneously incorporated as T_S noise forcing (Lee et al. 2008). This would result in an overestimate of intrinsic T_S variability shown in Fig. 5a. However, upon reconstructing the local-LIM with u (i.e. $\mathbf{x}(t) = [T_A(t) \ T_S(t) \ u(t)]^T$), which should serve as a good proxy for anomalous Ekman advection in the Kuroshio-Oyashio region, it is found that the amount of T_S noise forcing (Fig. 4c) and uncoupled T_S variability (Fig. 5a) is essentially unchanged (not shown). In fact, the main change due to the addition of u is in the dynamics of T_A , while leaving the *net* atmospheric impact on T_S unaltered. In short, the local-LIM implicitly includes the impact of u via T_A and thus, the subsequent impact this may have on dT_S/dt ; any remaining small

313 impact of u (and v) on T_S will be included in the noise.

314 A secondary caveat in our estimate of intrinsic T_S variability arises from the neglect
315 of removing the noise-induced drift. To the extent that all four coefficients in \mathbf{L} represent
316 wind-dependent fluxes, the coefficients should not be steady since the wind varies much
317 more rapidly than T_A or T_S , yielding state-dependent, or multiplicative, noise (Sura et al.
318 2006; Sura and Newman 2008). State-dependent noise simultaneously *weakens* coupling and
319 damping; for example, at Ocean Weathership (OWS) P, previously located in the Gulf of
320 Alaska, Sura and Newman (2008) estimate that this drift *reduces* the coupling strength by
321 about 30% and the SST damping rate by about 10%. Since multiplicative noise is state-
322 dependent, it should also be uncoupled. Using the values of the drift and noise obtained by
323 Sura and Newman (2008) for OWS P, uncoupling and eliminating all T_A -dependent noise
324 in the SST tendency equation results in a modest 5% reduction in retained SST variance.
325 Stated differently, our neglect of the noise-induced drift implies a slight overestimate of in-
326 trinsic SST variability. Of course, this estimate is for OWS P, and may be substantially
327 different in other parts of the basin.

328 *c) Air-sea coupling in fully coupled GCMs*

330 Recent studies have suggested that air-sea interaction on small scales may oppose the
331 BB98 paradigm in that SST anomalies force changes in the net surface heat flux through
332 modification of the boundary layer wind profile either by changing the low-level stability or
333 due to dynamical adjustment (Xie 2004; Samelson et al. 2006; Small et al. 2008). Coupled
334 modeling experiments by Bryan et al. (2010) further suggest that: (i) the fidelity to the
335 observed SST-wind stress relationship is greatly improved when an eddy-resolving ocean is
336 used, and (ii) for the version of CCSM3.5 with an eddy-resolving ocean model, increasing
337 atmospheric resolution provides no additional benefit. Thompson and Kwon (2010) and
338 Kirtman et al. (2012) suggest that the benefit of including ocean eddies also applies to
339 the larger-scale oceanic circulation, not just at the small-scale. Collectively, these findings

suggest that resolving ocean eddies enhances the realism in depicting air-sea interaction.

To test this hypothesis, we repeat the local-LIM analysis using two recent coupled GCM simulations from CCSM3.5 (Gent et al. 2010) that only differ in their oceanic model resolution. The HR (LR) simulation has an ocean model resolution of 0.1° (1.0°); both employ the 0.5° Community Atmosphere Model version 3 for the atmosphere. Note the HR allows for oceanic eddies, which are parameterized by the large-scale flow in the LR. Figure 6a,b shows the standard deviation of weekly SST anomalies in the LR and HR, respectively. The LR displays a commonly known northward bias in the WBC separation shown by other lower resolution models (Thompson and Kwon 2010), with the maximum WBC SST variability located around 43°N in Fig. 6a compared to around 38°N in Fig. 1a. In contrast, the HR reproduces the latitude of maximum variability better, but shows substantially too much SST variability basin-wide (Fig. 6b) and appears to be less successful than the LR in representing variability in the ENSO teleconnection/subtropical front region near 35°N , 150°W . Both models reproduce the amplitude and structure of T_A variance very well (not shown). Figure 2e-l shows the coefficients of \mathbf{L} obtained for both GCM simulations. Both GCMs capture the structure and amplitude of the T_A damping (a) and the relative increase in T_S damping in the subtropics, but both also underestimate the T_S damping (d) and the T_A effect on T_S (c). Meanwhile, uncoupling \mathbf{L} from the HR and LR local-LIMs yields quite different results: in the LR simulation, there is very little SST variability that is not generated by the atmosphere (Fig. 6c), while 60-80% of SST variability in the HR is independent of the atmosphere over large portions of the western North Pacific (Fig. 6d). This stark difference appears to be due to different T_S noise forcing for each model (Fig. 6e,f), since compared to observations (cf. Fig. 4c), HR overestimates T_S noise forcing within the WBC by a factor of 5, while LR grossly underestimates it. No such difference exists for the models' T_A noise forcing, which is comparable to observations (not shown).

4. The importance of non-local factors

The benefit of using a local model is its simplicity, but one potential concern is that the local-LIM might convolve non-local processes in the coefficients contained within \mathbf{L} , as would occur if coefficient a (d) had a dependence on ∇T_A (∇T_S). For example, consider the non-local interaction as depicted schematically in Fig. 7 for two hypothetical regions A and B. The coefficients of the local-LIM (Fig. 2) are meant to represent processes 1-4 ($a \rightarrow 1$, $d \rightarrow 2$, $c \rightarrow 3$, $b \rightarrow 4$) in Fig. 7, which portray radiative and thermal heat flux anomalies as posited by BB98. But the a - d coefficients may also implicitly represent non-local processes 5-12 especially in regions where advection is important (e.g. WBC). Additionally, processes 7-10 in Fig. 7 represent the indirect remote interaction of T_A and T_S through changes in ∇T_A , ∇T_S , cloud cover, wind or moisture anomalies that are not represented by the local-LIM but may improve the non-local model's predicted covariance.

We explore explicitly resolving non-local interactions in this section by constructing a LIM from a multidimensional state vector consisting of anomalies averaged within certain regions, or boxes, following Shin et al. (2010). The boxes are chosen based on: (i) SST variance (Fig. 1a) and (ii) the patterns of the leading two empirical orthogonal functions (EOFs) of weekly wintertime North Pacific (20-65°N) SST anomalies. The two EOFs, which are the only statistically separable ones and explain a combined 43% of the variance, are shown in Fig. 8 along with the boxes. T_S and T_A anomalies are averaged within each box to create the state vector, \mathbf{X}^B . Each box contains the same amount of grid points, but note that variability in the west may have smaller-scale, higher-frequency features (see Hosoda and Kawamura 2005). We estimate the dynamical operator \mathbf{B} (to distinguish from \mathbf{L} in the local-LIM) through (A1) using the same procedure as for \mathbf{L} (7-day running mean, $\tau = 7$ days). Then \mathbf{B} is used to generate the predicted lag-covariance out to 90 days through (A2). Hereafter, we refer to the non-local LIM as the box-LIM. For direct comparison, we also fit a local-LIM separately to each box denoting the resulting operators \mathbf{L}^B . We can then explore whether the local-LIM adequately represents the additional complexity of the box-LIM and in particular, the extent to which the dynamics and coupling are truly local.

We first address how the number of boxes contained in $\mathbf{X}^{\mathbf{B}}$ affects forecast skill. We design five experiments, shown in Table 1, by varying the combination of boxes that comprise $\mathbf{X}^{\mathbf{B}}$ from a total of 2 to 5. Experiment 1 starts by using just two boxes, 1 and 4, which are used in all the other experiments. Figure 9 illustrates the impact of adding additional boxes with the 1-90 day forecast skill of T_S at boxes 1 (Gulf of Alaska) and 4 (WBC region) for all experiments. Additionally, Table 1 shows the day 90 skill for T_S and T_A . The skill is cross-validated using independent data as outlined in Winkler et al. (2001). Figure 9 shows a general increase in skill, mainly in Box 1, as additional boxes are added. However, the increase is not steady as it is most rapid from Exp1 through 3, but negligible once $\mathbf{X}^{\mathbf{B}}$ contains more than four boxes. Several four-box variations of $\mathbf{X}^{\mathbf{B}}$, with and without boxes 1 and 4, support this (not shown). Of all boxes, Box 4 skill shows the least improvement with the addition of more boxes, implying that its dynamics are less affected by remote interaction though it is still important in elevating the skill of other boxes (such as Box 1).

We evaluate the box-LIM further by comparing it to the local-LIM. Figure 10 shows the 1-90 day skill across all boxes for T_S and T_A using \mathbf{B} from Exp3 and $\mathbf{L}^{\mathbf{B}}$ for each box, as a pattern anomaly correlation with observations. We use Exp3 since it captures almost all the skill achievable from the box-LIM. Adding non-local interaction boosts skill in both T_S and T_A forecasts. Although this is true for all boxes (not shown), the effect is relatively larger in boxes 1,3 (not shown). Next, we recalculate skill after isolating the local processes of \mathbf{B} (setting all non-local processes to zero) and denoting this operator \mathbf{B}^{1d} , shown in Fig. 10. The skill using \mathbf{B}^{1d} is worse than $\mathbf{L}^{\mathbf{B}}$ for both T_A and T_S , implying that the local-LIM coefficients a - d implicitly incorporate some non-local processes. Separately suppressing remote T_A (processes 5,6 in Fig. 7) and T_S (processes 11,12) interactions indicates the absence of remote T_A interaction is responsible for most of the skill degradation (not shown), which is physically plausible on the relatively short timescales we consider.

Finally, we investigate whether the local-LIM and box-LIM differ in their treatment of coupling. The observed and predicted lagged cross-covariance using \mathbf{B} and $\mathbf{L}^{\mathbf{B}}$ is shown in

Fig. 11 for boxes 3 (east-central North Pacific) and 4 (WBC region). In both boxes, the cross-covariance is maximized when T_A leads T_S by 5-7 days, as expected when T_A forces T_S . However, even though weekly T_S and T_A variability is comparable between boxes 3 and 4 (cf. Fig. 1a,b), the cross-covariance is much higher at box 3 across all lags, implying a much stronger local coupling here. In box 4 (Fig. 11b), the local-LIM and box-LIM both predict the cross-covariance within the 95% confidence range based on 200 iterations of a Monte Carlo simulation, though both underestimate the cross-covariance when T_S leads by more than 60 days. Meanwhile, the box-LIM outperforms the local-LIM at box 3 (Fig. 11a), though both underestimate the magnitude of the cross-covariance. Note that box 3 has a well-documented ENSO teleconnection that may explain the difference between the box-LIM and local-LIM prediction there. Lastly, we solve the fluctuation-dissipation relation (A3) by removing all processes that represent coupling in \mathbf{B} and $\mathbf{L}^{\mathbf{B}}$, denoting the uncoupled operators \mathbf{B}^u and $\mathbf{L}^{\mathbf{B},u}$, respectively. Figure 12 shows that the fraction of retained T_S variance is nearly identical between the box-LIM and local-LIM, and also confirms that the WBC region (box 4) has substantially more uncoupled SST variance relative to the other boxes. There are some minor discrepancies between uncoupled T_A variance among boxes, but this disappears upon averaging over all boxes and could be due to uncertainties in the coefficients of \mathbf{B} and $\mathbf{L}^{\mathbf{B}}$.

5. Conclusions

A coupled local-LIM of T_A and T_S fit to observations predicts lagged covariance statistics well on timescales up to a season. The main additions to the findings of BB98 are: (i) the model does surprisingly well in dynamically active oceanic regions but only with the inclusion of a substantial amount of T_S noise forcing and (ii) *local* coupling varies very strongly over the basin, generally being more important as one moves east across the North Pacific. Uncoupling the model's simple dynamics results in a near complete elimination of SST variability everywhere away from the WBC region, while T_A variability is only slightly

affected. In the WBC region, $\sim 50\%$ of monthly T_S variability appears intrinsic to the ocean. It is important to recall that our use of the term coupling does not differentiate between the relative magnitude of T_S versus T_A forcing, as even in a strongly coupled region like the eastern North Pacific, nearly all SST variability is driven by T_A . Thus, in this context and in BB98, strong coupling mainly drives an increase in the persistence of T_A and T_S anomalies.

We apply the same analysis to two coupled GCMs using the same atmospheric GCM but either a high (0.1°) or low (1.0°) resolution ocean model. We find that the 0.1° model generates more SST variability compared to the 1.0° model and observations, but better reproduces the latitude of maximum variability within the WBC (cf. Fig. 1a with Fig. 6a,b). By uncoupling \mathbf{L} in the local-LIM of each GCM, we find the 0.1° ocean model shows substantially more intrinsic SST variability within the WBC compared to the 1° model. This difference is partially explained by the near absence of T_S noise forcing within the 1° , while the 0.1° model generally overestimates this quantity within the WBC (cf. Fig. 4a and 6e,f). Though the large overestimate of T_S variance within 0.1° model is certainly a caveat that makes it difficult to choose one GCM as superior over the other, it is clear that resolving ocean eddies properly in future coupled GCMs will likely yield a significant impact on their depiction of air-sea interaction.

We remove the 1-D constraint of the local-LIM by creating a box-LIM based on area-averaged T_A and T_S anomalies located in regions of high SST variance (Fig. 8). The skill of the box-LIM shows improvement over its local-LIM equivalent in both T_S and T_A . However, subsequent modification of the box-LIM to remove non-local interaction shows a substantial drop in skill, suggesting that the local-LIM coefficients implicitly incorporate some non-local processes (Fig. 10). Furthermore, the role of non-local interaction affects the eastern boxes more than those in the west, likely due to a significant portion of ENSO forcing that is not explicitly represented by our box-LIM framework. A logical next step is to explicitly include the tropical Pacific into the state vector \mathbf{X}^B as in Newman et al. (2003). Meanwhile, concerning coupling, the box-LIM and local-LIM yield nearly identical results (Fig. 12).

Finally, the concept of “retained” SST variance deserves some discussion. In the purely passive model of BB98, there is no retained SST variability if the dynamics are uncoupled. For this reason, extreme caution was suggested in the design of SST-forced AGCM experiments. The results herein suggest that enough independent SST variability exists within the WBC region so that it is not unreasonable to prescribe SST anomalies there. This supports the approach of experiments by Yulaeva et al. (2001), Liu and Wu (2004), Minobe et al. (2008) and Kwon et al. (2011), all of which target the WBC by forcing with either SST, oceanic heat flux convergence or oceanic mixed-layer heat content anomalies. Note, however, that even in this region, $\sim 50\%$ of SST variability is coupled to the atmosphere, so the problem of forcing an atmospheric GCM with T_A -driven SST anomalies cannot be ignored. Even though we have shown that regions within the WBC experience ocean-driven SST variability, the methods in this study are insufficient in determining how these “retained” anomalies influence the atmosphere. Clearly, Fig. 5b suggests the atmospheric response must be significantly non-local, as alluded to by Frankignoul et al. (2011) and Taguchi et al. (2012). Higher-order models are currently being developed to determine whether the intrinsic SST anomalies exert a simple boundary layer atmospheric response that is quickly overridden with intrinsic atmospheric variability, or a deeper response that could potentially influence large scale atmospheric modes, possibly leading to longer-term predictability.

Acknowledgments.

The authors thank J. Barsugli, C. Frankignoul, D. Vimont, F. Bryan and three anonymous reviewers for insightful comments. C. Hannay (NCAR) helped in acquiring the CCSM4 output. Funding for DS and MN was provided by NSF grant 1035423.

Estimating the LIM coefficients

Using LIM, we assume a stochastically forced system with stationary statistics and dynamics that are linear, or can be approximated as linear functions of T_A and T_S (Sura and Newman 2008). Intuitively, T_A and T_S are chosen because T_S variability largely depends on the net turbulent heat flux (F_{net}) in which T_A is a dominant factor (Cayan 1992; Alexander and Scott 1997). Other variables that are important to F_{net} , such as specific humidity, can to some degree be parameterized as a function of T_A . After solving the discretized form of (2) for $\mathbf{x}(t)$, multiplying the result by $\mathbf{x}(t + \tau)$ [where τ is a lag time of 7 days] and taking the expectation (denoted by $\langle \rangle$), \mathbf{L} is estimated as:

$$\mathbf{L} = \frac{1}{\tau} \ln [\mathbf{C}(\tau)\mathbf{C}(0)^{-1}] \quad (\text{A1})$$

where $\mathbf{C}(\tau) = \langle \mathbf{x}(t+\tau)\mathbf{x}(t)^T \rangle$ is the τ -lag covariance and $\mathbf{C}(0) = \langle \mathbf{x}(t)\mathbf{x}(t)^T \rangle$ is the zero-lag covariance. The choice of τ is relatively subjective but it is a key test of the LIM to consider a range of τ and verify that \mathbf{L} does not significantly change (Penland and Sardeshmukh 1995). However, when altering τ , it is sometimes necessary to filter the data to remove very high frequency variability. We use a range of $\tau=[1,3,5,7,11,15,21]$ and accordingly, a boxcar filter of the same length as τ to smooth \mathbf{x} . For $\tau < 7$ days, \mathbf{L} is not constant; on the other hand, \mathbf{L} is nearly unchanged for $\tau > 7$, so we set $\tau = 7$.

Since the noise forcing in (2) is unpredictable, the most likely evolution of $\mathbf{x}(t)$ at time $t + \tau$ is (Penland and Sardeshmukh 1995):

$$\mathbf{x}(t + \tau) = \exp(\mathbf{L}\tau)\mathbf{x}(t). \quad (\text{A2})$$

518 Eigenanalysis of \mathbf{L} yields eigenvectors and potentially complex eigenvalues, which together
 519 characterize the eigenmodes of (A2) (Penland 1996; Penland and Sardeshmukh 1995). For
 520 the local-LIM, we have two eigenmodes and find that the accompanying eigenvalues are real
 521 and negative, implying anomaly decay to climatology over a finite time. This is not true for
 522 the box-LIM, which has several complex eigenmodes, though all have negative real parts.

523 The LIM explains the balance of external forcing, ξ , that is constantly being damped
 524 back towards climatology by \mathbf{L} , which is quantified by the fluctuation-dissipation relation
 525 (FDR; Penland and Matrosova 1994):

$$\frac{d\mathbf{C}(0)}{dt} = \mathbf{L}\mathbf{C}(0) + \mathbf{C}(0)\mathbf{L}^T + \mathbf{Q} = 0. \quad (\text{A3})$$

526 where $\mathbf{Q} = \langle \xi \xi^T \rangle dt$ (Penland 1996), or:

$$\mathbf{Q} = \begin{bmatrix} \langle \xi_A \xi_A \rangle & \langle \xi_A \xi_S \rangle \\ \langle \xi_S \xi_A \rangle & \langle \xi_S \xi_S \rangle \end{bmatrix} dt,$$

528 where $\xi_A(\xi_S)$ represents the T_A (T_S) noise forcing, and the diagonal elements of \mathbf{Q} are
 529 referred to as the T_A (T_S) noise covariance, \mathbf{Q}_A (\mathbf{Q}_S), respectively.

530 In practice, \mathbf{L} is determined through (A1) and \mathbf{Q} is determined as a residual in (A3)
 531 under the assumption that the system's statistics are stationary, $d\mathbf{C}(0)/dt = 0$ (Penland
 532 1996). Additionally, \mathbf{L} and \mathbf{Q} can depend on the annual cycle, which can influence the
 533 quality of the forecast in (A2) (Penland and Ghil 1993). We recalculate \mathbf{L} and \mathbf{Q} using
 534 all months and just warm months (Apr-Oct) and note at least two substantial differences
 535 between the winter-only LIM. First, the summer LIM has a generally weaker \mathbf{Q} consistent
 536 with reduced atmospheric variability during the warm months. Second, the model skill is
 537 lower, likely due to the elevated role non-linear effects such as cloud-cover (e.g. Park et al.
 538 2006) in dictating SST variability during the summer. Finally, it is notable that the local
 539 noise approximation of BB98 and FH77 holds relatively well, as the off-diagonal elements of

540 **Q** contribute little to the FDR balance (not shown).

REFERENCES

- 543 Alexander, M., I. Bladé, M. Newman, J. Lanzante, N. Lau, and J. Scott, 2002: The at-
 544 mospheric bridge: The influence of ENSO teleconnections on air-sea interaction over the
 545 global oceans. *J. Climate*, **15**, 2205–2232.
- 546 Alexander, M. and C. Deser, 1995: A mechanism for the recurrence of wintertime midlatitude
 547 SST anomalies. *J. Phys. Oceanogr.*, **25**, 122–137.
- 548 Alexander, M., J. Scott, and C. Deser, 2000: Processes that influence sea surface temperature
 549 and ocean mixed layer depth variability in a coupled model. *J. Geophys. Res.*, **105**, 16.
- 550 Alexander, M. and J. Scott, 1997: Surface flux variability over the North Pacific and North
 551 Atlantic oceans. *J. Climate*, **10**, 2963–2978.
- 552 Alexander, M., 1992: Midlatitude atmosphere–ocean interaction during El Niño. Part I: The
 553 North Pacific Ocean. *J. Climate*, **5**, 944–958.
- 554 Alexander, M., 2010: Extratropical air-sea interaction, SST Variability and the Pacific
 555 Decadal Oscillation. *Climate Dynamics: Why Does Climate Vary?*, **189**, 123–148.
- 556 Barsugli, J. and D. Battisti, 1998: The Basic Effects of Atmosphere-Ocean Thermal Coupling
 557 on Midlatitude Variability. *J. Atmos. Sci.*, **55**, 477–493.
- 558 Bjerknes, J., 1964: Atlantic air-sea interaction. *Advances in Geophysics*, **10**, 82.
- 559 Brayshaw, D., B. Hoskins, and M. Blackburn, 2009: The basic ingredients of the North
 560 Atlantic storm track. Part I: Land-sea contrast and orography. *J. Atmos. Sci.*, **66**, 2539–
 561 2558.

- Brayshaw, D., B. Hoskins, and M. Blackburn, 2011: The basic ingredients of the North Atlantic storm track. Part II: Sea surface temperatures. *J. Atmos. Sci.*, **68**, 1784–1805.
- Bretherton, C. and D. Battisti, 2000: Interpretation of the results from atmospheric general circulation models forced by the time history of the observed sea surface temperature distribution. *Geophys. Res. Lett.*, **27**, 767–770.
- Bryan, F., R. Tomas, J. Dennis, D. Chelton, N. Loeb, and J. McClean, 2010: Frontal scale air-sea interaction in high-resolution coupled climate models. *J. Climate*, **23**, 6277–6291.
- Cayan, D., 1992: Latent and sensible heat flux anomalies over the northern oceans: Driving the sea surface temperature. *J. Phys. Oceanogr.*, **22**, 859–881.
- Chelton, D., M. Schlax, M. Freilich, and R. Milliff, 2004: Satellite measurements reveal persistent small-scale features in ocean winds. *Science*, **303**, 978–983.
- Deser, C., M. Alexander, and M. Blackmon, 1999: Evidence for a wind-driven intensification of the kuroshio current extension from the 1970s to the 1980s. *J. Climate*, **12**, 1697–1706.
- Diaz, H., M. Hoerling, and J. Eischeid, 2001: ENSO variability, teleconnections and climate change. *Int. J. of Climatology*, **21**, 1845–1862.
- Dong, S. and K. A. Kelly, 2004: Heat budget in the gulf stream region: The importance of heat storage and advection. *Journal of Physical Oceanography*, **34**, 1214–1231.
- Ferranti, L., F. Molteni, and T. Palmer, 1994: Impact of localized tropical and extratropical SST anomalies in ensembles of seasonal GCM integrations. *Quart. J. Roy. Met. Soc.*, **120**, 1613–1645.
- Frankignoul, C. and K. Hasselmann, 1977: Stochastic climate models, part II: Application to sea-surface temperature anomalies and thermocline variability. *Tellus*, **29**, 289–305.
- Frankignoul, C. and E. Kestenare, 2002: The surface heat flux feedback. Part I: Estimates from observations in the Atlantic and the North Pacific. *Clim. Dyn.*, **19**, 633–647.

- Frankignoul, C. and R. Reynolds, 1983: Testing a dynamical model for mid-latitude sea surface temperature anomalies. *J. Phys. Oceanogr.*, **13**, 1131–1145.
- Frankignoul, C., N. Sennéchal, Y. Kwon, and M. Alexander, 2011: Influence of the Meridional Shifts of the Kuroshio and the Oyashio Extensions on the Atmospheric Circulation. *J. Climate*, **24** (762–777).
- Frankignoul, C., 1985: Sea surface temperature anomalies, planetary waves, and air-sea feedback in the middle latitudes. *Reviews of geophysics*, **23**, 357–390.
- Gent, P., S. Yeager, R. Neale, S. Levis, and D. Bailey, 2010: Improvements in a half degree atmosphere/land version of the CCSM. *Clim. Dyn.*, **34**, 819–833.
- Gent, P., et al., 2011: The Community Climate System Model, version 4. *J. Climate*, **24**, 4973–4991.
- Hall, A. and S. Manabe, 1997: Can local linear stochastic theory explain sea surface temperature and salinity variability? *Clim. Dyn.*, **13**, 167–180.
- Hoerling, M. and A. Kumar, 2002: Atmospheric response patterns associated with tropical forcing. *J. Climate*, **15**, 2184–2203.
- Hosoda, K. and H. Kawamura, 2005: Seasonal variation of space/time statistics of short-term sea surface temperature variability in the Kuroshio region. *Journal of Oceanography*, **61**, 709–720.
- Kelly, K., 2004: The relationship between oceanic heat transport and surface fluxes in the western North Pacific: 1970–2000. *J. Climate*, **17**, 573–588.
- Kirtman, B., et al., 2012: Impact of ocean model resolution on CCSM climate simulations. *Clim. Dyn.*, 1–26.
- Kossin, J. and D. Vimont, 2007: A more general framework for understanding Atlantic hurricane variability and trends. *Bull. Amer. Met. Soc.*, **88**, 1767–1782.

- Kushnir, Y. and I. Held, 1996: Equilibrium atmospheric response to North Atlantic SST anomalies. *J. Climate*, **9**, 1208–1220.
- Kushnir, Y., W. Robinson, I. Bladé, N. Hall, S. Peng, and R. Sutton, 2002: Atmospheric GCM Response to Extratropical SST Anomalies: Synthesis and Evaluation*. *J. Climate*, **15**, 2233–2256.
- Kwon, Y., M. Alexander, N. Bond, C. Frankignoul, H. Nakamura, B. Qiu, and L. Thompson, 2010: Role of the Gulf Stream and Kuroshio-Oyashio Systems in Large-Scale Atmosphere-Ocean Interaction: A Review. *J. Climate*, **23**, 3249–3281.
- Kwon, Y., C. Deser, and C. Cassou, 2011: Coupled atmosphere–mixed layer ocean response to ocean heat flux convergence along the Kuroshio Current Extension. *Climate Dynamics*, **36 (11)**, 2295–2312.
- Lee, D., Z. Liu, and Y. Liu, 2008: Beyond Thermal Interaction between Ocean and Atmosphere: On the Extratropical Climate Variability due to the Wind-Induced SST. *J. Climate*, **21**, 2001–2018.
- Liu, Z. and L. Wu, 2004: Atmospheric Response to North Pacific SST: The Role of Ocean-Atmosphere Coupling. *J. Climate*, **17**, 1859–1882.
- Miller, A. J., D. R. Cayan, T. P. Barnett, N. E. Graham, and J. M. Oberhuber, 1994: Interdecadal variability of the pacific ocean: Model response to observed heat flux and wind stress anomalies. *Climate Dynamics*, **9 (6)**, 287–302.
- Minobe, S., A. Kuwano-Yoshida, N. Komori, S. Xie, and R. Small, 2008: Influence of the Gulf Stream on the troposphere. *Nature*, **452 (7184)**, 206–209.
- Mitsudera, H., B. Taguchi, Y. Yoshikawa, H. Nakamura, T. Waseda, and T. Qu, 2004: Numerical Study on the Oyashio Water Pathways in the Kuroshio-Oyashio Confluence. *J. Phys. Oceanography*, **34**, 1174–1196.

- Mosedale, T., D. Stephenson, and M. Collins, 2005: Atlantic atmosphere-ocean interaction: a stochastic climate model-based diagnosis. *J. Climate*, **18**, 1086–1095.
- Nakamura, H., G. Lin, and T. Yamagata, 1997: Decadal climate variability in the North Pacific during the recent decades. *Bull. Amer. Meteor. Soc.*, **78**, 2215–2225.
- Nakamura, H., T. Sampe, A. Goto, W. Ohfuchi, and S. Xie, 2008: On the importance of midlatitude oceanic frontal zones for the mean state and dominant variability in the tropospheric circulation. *Geophys. Res. Lett.*, **35**, L15 709.
- Nakamura, H., T. Sampe, Y. Tanimoto, and A. Shimpo, 2004: Observed associations among storm tracks, jet streams and midlatitude oceanic fronts. *Geophysical Monograph Series*, **147**, 329–345.
- Namias, J., 1959: Recent seasonal interactions between north pacific waters and the overlying atmospheric circulation. *J. Geophys. Res.*, **64**, 631–646.
- Newman, M., P. Sardeshmukh, C. R. Winkler, and J. S. Whitaker, 2003: A Study of Sub-seasonal Predictability. *Mon. Wea. Rev.*, **131**, 1715–1732.
- Nonaka, M., H. Nakamura, B. Taguchi, N. Komori, A. Kuwano-Yoshida, and K. Takaya, 2009: Air-sea heat exchanges characteristic of a prominent midlatitude oceanic front in the south Indian Ocean as simulated in a high-resolution coupled GCM. *J. Climate*, **22**, 6515–6535.
- North, G., T. Bell, R. Cahalan, and F. Moeng, 1982: Sampling errors in the estimation of empirical orthogonal functions. *Mon. Wea. Rev.*, **110**, 699–706.
- Park, S., M. Alexander, and C. Deser, 2006: The impact of cloud radiative feedback, remote ENSO forcing, and entrainment on the persistence of North Pacific sea surface temperature anomalies. *J. Climate*, **19**, 6243–6261.

- 657 Park, S., C. Deser, and M. Alexander, 2005: Estimation of the surface heat flux response to
658 sea surface temperature anomalies over the global oceans. *J. Climate*, **18**, 4582–4599.
- 659 Pegion, K. and P. Sardeshmukh, 2011: Prospects for Improving Subseasonal Predictions.
660 *Mon. Wea. Rev.*, **139**, 3648–3666.
- 661 Peng, S., L. Mysak, H. Ritchie, J. Derome, and B. Dugas, 1995: The Differences between
662 Early and Midwinter Atmospheric Responses to Sea Surface Temperature Anomalies in
663 the Northwest Atlantic. *J. Climate*, **8**, 137–157.
- 664 Peng, S., W. Robinson, and M. Hoerling, 1997: The Modeled Atmospheric Response to
665 Midlatitude SST Anomalies and Its Dependence on Background Circulation States. *J.*
666 *Climate*, **10**, 971–987.
- 667 Penland, C. and M. Ghil, 1993: Forecasting Northern Hemisphere 700-mb geopotential
668 height anomalies using empirical normal modes. *Mon. Wea. Rev.*, **121**, 2355–2372.
- 669 Penland, C. and L. Matrosova, 1994: A Balance Condition for Stochastic Numerical Models
670 with Application to the El Nino-Southern Oscillation. *J. Climate*, **7**, 1352–1372.
- 671 Penland, C. and P. Sardeshmukh, 1995: The optimal growth of tropical sea surface temper-
672 ature anomalies. *J. Climate*, **8**, 1999–2024.
- 673 Penland, C., 1989: Random forcing and forecasting using principal oscillation pattern anal-
674 ysis. *Mon. Wea. Rev.*, **117** (10), 2165–2185.
- 675 Penland, C., 1996: A stochastic model of IndoPacific sea surface temperature anomalies.
676 *Physica D: Nonlinear Phenomena*, **98**, 534–558.
- 677 Qiu, B., 2000: Interannual variability of the Kuroshio Extension system and its impact on
678 the wintertime SST field. *J. Phys. Oceanography*, **30**, 1486–1502.
- 679 Reynolds, R., 1978: Sea surface temperature anomalies in the North Pacific Ocean. *Tellus*,
680 **30**, 97–103.

- Samelson, R., E. Skyllingstad, D. Chelton, S. Esbensen, L. O'Neill, and N. Thum, 2006: On the coupling of wind stress and sea surface temperature. *J. Climate*, **19**, 1557–1566.
- Saravanan, R., 1998: Atmospheric low-frequency variability and its relationship to midlatitude SST variability: Studies using the NCAR Climate System Model. *J. Climate*, **11** (6), 1386–1404.
- Schneider, N., A. Miller, and D. Pierce, 2002: Anatomy of north pacific decadal variability. *J. Climate*, **15**, 586–605.
- Shin, S., P. Sardeshmukh, and K. Pegion, 2010: Realism of local and remote feedbacks on tropical sea surface temperatures in climate models. *J. Geophys. Res.*, **115**, D21 110.
- Small, R., et al., 2008: Air–sea interaction over ocean fronts and eddies. *Dynamics of Atmospheres and Oceans*, **45**, 274–319.
- Sura, P., M. Newman, and M. Alexander, 2006: Daily to Decadal Sea Surface Temperature Variability Driven by State-Dependent Stochastic Heat Fluxes. *J. Phys. Oceanogr.*, **36**, 1940–1958.
- Sura, P. and M. Newman, 2008: The impact of rapid wind variability upon air-sea thermal coupling. *J. Climate*, **21**, 621–637.
- Sutton, R. and P. Mathieu, 2002: Response of the ocean-atmosphere mixed-layer system to anomalous heat-flux convergence. *Quart. J. Roy. Met. Soc.*, **128**, 1259–1275.
- Taguchi, B., H. Nakamura, M. Nonaka, N. Komori, A. Kuwano-Yoshida, K. Takaya, and A. Goto, 2012: Seasonal evolutions of atmospheric response to decadal sst anomalies in the north pacific subarctic frontal zone: Observations and a coupled model simulation. *J. Climate*, **25**, 111–139.
- Taguchi, B., H. Nakamura, M. Nonaka, and S. Xie, 2009: Influences of the Kuroshio/Oyashio

704 Extensions on Air-Sea Heat Exchanges and Storm-Track Activity as Revealed in Regional
705 Atmospheric Model Simulations for the 2003/04 Cold Season. *J. Climate*, **22**, 6536–6560.

706 Thompson, L. and Y. Kwon, 2010: An Enhancement of Low-Frequency Variability in the
707 Kuroshio-Oyashio Extension in CCSM3 owing to Ocean Model Biases. *Journal of Climate*,
708 **23**, 6221–6233.

709 Winkler, C., M. Newman, and P. Sardeshmukh, 2001: A Linear Model of Wintertime Low-
710 Frequency Variability. Part I: Formulation and Forecast Skill. *J. Climate*, **14**, 4474–4494.

711 Xie, S., 2004: Satellite Observations of Cool Ocean-Atmosphere Interaction*. *Bull. Amer.*
712 *Meteor. Soc.*, **85**, 195–208.

713 Yulaeva, E., N. Schneider, D. Pierce, and T. Barnett, 2001: Modeling of North Pacific
714 climate variability forced by oceanic heat flux anomalies. *J. Climate*, **14**, 4027–4046.

715 Yu, L. and R. Weller, 2007: Objectively analyzed air-sea heat fluxes for the global ice-free
716 oceans (1981-2005). *Bull. Amer. Meteor. Soc.*, **88**, 527–539.

717 Zubarev, A. and P. Demchenko, 1992: Predictability of averaged global air temperature in
718 a simple stochastic atmospheric-ocean interaction model. *Isv. Atmos. Oceanic Phys*, **28**,
719 19–23.

List of figures

Figure 1: Standard deviation of (a) weekly-averaged TS, (b) weekly- and (c) daily-averaged TA anomalies from OAFlux, extended winter only (NDJFM). TS variability is essentially unchanged when averaging daily to weekly to monthly. Weekly average TA is shown because a 7-day running mean is used in the LIM.

Figure 2: Spatial variability of the coefficients in the dynamical operator L, found separately for every grid point using (a-d) OAFlux observations and (e-h) LR and (i-l) HR model output. See Section 3c for the details of the model configurations. The top (bottom) colorbar corresponds to the top (bottom) two rows. Coefficients a, d represent damping rate (days^{-1}) of T_A (T_S), while coefficients b, c represent coupling strength (b : $T_S \rightarrow T_A$ and c : $T_A \rightarrow T_S$).

Figure 3: The observed (shading) lag-covariance for T_S (a,c,e) and T_A (b,d,f) when τ equals (a,b) 30 days, (c,d) 60 days, (e,f) 90 days. The contour encloses areas where the difference between the observed lag covariance and that predicted by the local-LIM exceeds the $p=0.025$ confidence level from a Monte Carlo test. Note that the local-LIM generally underestimates lagged covariance.

Figure 4: (a) The normalized power spectra of T_S (black), η_A (red), and η_S (blue) for 20 randomly sampled points, shown as black dots in (c) over the North Pacific. Note that η is determined using a finite differencing approximation shown in (6). The ω^{-2} line is shown to reference an undamped Markov model. For clarity, η_A (η_S) has been scaled by 0.03 (0.003). Thus, the values on the y-axis are only relative and should be used to note the ω -dependence of each spectrum. The noise covariance (Q) of (b) T_A and (c) T_S calculated through (A3) separately at every grid point using L and the observed covariance structure.

Figure 5: The fractional amount of retained (a) monthly averaged T_S and (b) total T_A vari-

ability after integrating (2) with the uncoupled operator L^u and noise Q^u .

Figure 6: (a & b) Standard deviation of weekly averaged, extended winter (NDJFM) TS anomalies from CCSM3.5 with an ocean model resolution of (a) 1° (LR) and (b) 0.1° (HR). These can be directly compared to Fig 1a. The white contours in (b) denote values exceeding the colorbar with a 0.2°C increment. (c & d) Same as Fig. 5a except for (c) LR and (d) HR. (e & f) Same as Fig. 4b except for (e) LR and (f) HR. The white contours in (f) denote values exceeding the colorbar with a $0.02^\circ\text{C}^2 \text{ day}^{-1}$ increment.

Figure 7: Schematic of interactions in a hypothetical T_A , T_S coupled model of two boxes, A and B. Processes are arbitrarily labeled for use within the discussion.

Figure 8: The leading two EOFs of weekly averaged, wintertime (NDJFM) SST anomalies over the North Pacific ($20\text{-}60^\circ\text{N}$, 120°E - 120°W). Boxes indicate the averaging regions used to build the box-LIM (see text). Values in the top right show the percent of variance explained by the EOF. Note that only these two EOFs are statistically separable using the technique of North et al. (1982).

Figure 9: (a) Cross-validated skill as a function of lead-time for Box 1 and Box 4 T_S (anomaly correlation with observations) using B from the five experiments shown in Table 1. The black dots indicate the day 90 skill of Box 1 and 4 in the local-LIM. Box 1, the dashed line showing the skill of exp3 is masked by the solid line showing exp4.

Figure 10: Cross-validated pattern anomaly correlation with observations of T_S and T_A using B (solid), L^B (dash) and B^{1d} (dotted) from Exp3.

Figure 11: Observed (solid), and predicted (dash: using B from exp3; dotted: using L^B)

lag cross-covariance between T_S and T_A as a function of lag time for (a) box 3 (east-central Pacific), and (b) box 4 (WBC region). T_A leads (lags) T_S when the lag time is negative (positive). Gray crosses indicate the upper (97.5%) and lower (2.5%) ranges using 200 iterations of a Monte Carlo test.

Figure 12: (Bottom) The fraction of T_S and T_A variance retained after uncoupling B (from Exp3, black) and L^B (gray) at every box. Also shown is the average across all boxes for T_S and T_A .

Exp	Boxes used	Day 90 skill (Box 1)		Day 90 skill (Box 4)	
		T_S	T_A	T_S	T_A
1	1, 4	0.60 (0.63)	0.42 (0.30)	0.47 (0.45)	0.23 (0.12)
2	1, 2, 4	0.68	0.49	0.47	0.23
3	1-4	0.71	0.52	0.49	0.24
4	1-5	0.71	0.52	0.48	0.24
5	1-4, 6	0.73	0.54	0.49	0.23

Table 1: Box-LIM experiments 1-5 constructed by building the state vector \mathbf{X}^B from the specified boxes (see Fig. 8). Also shown is the 90-day cross-validated forecast skill, as an anomaly correlation, at boxes 1 and 4. The cross-validated 90-day local-LIM skill is shown in parentheses.

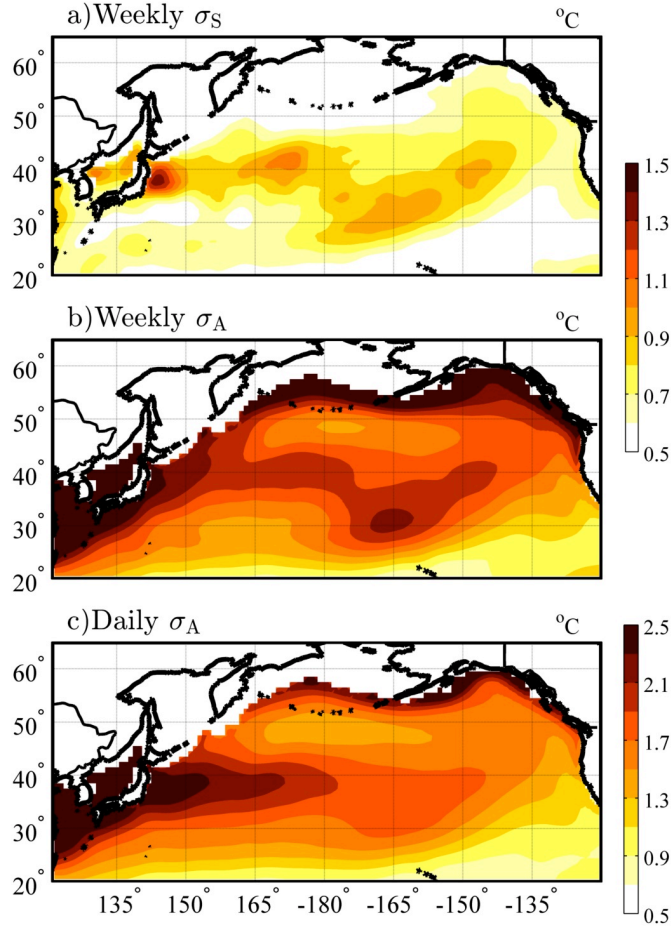


Figure 1: Standard deviation of (a) weekly-averaged T_S , (b) weekly- and (c) daily-averaged T_A anomalies from OAFflux, extended winter only (NDJFM). T_S variability is essentially unchanged when averaging daily to weekly to monthly. Weekly average T_A is shown because a 7-day running mean is used in the LIM.

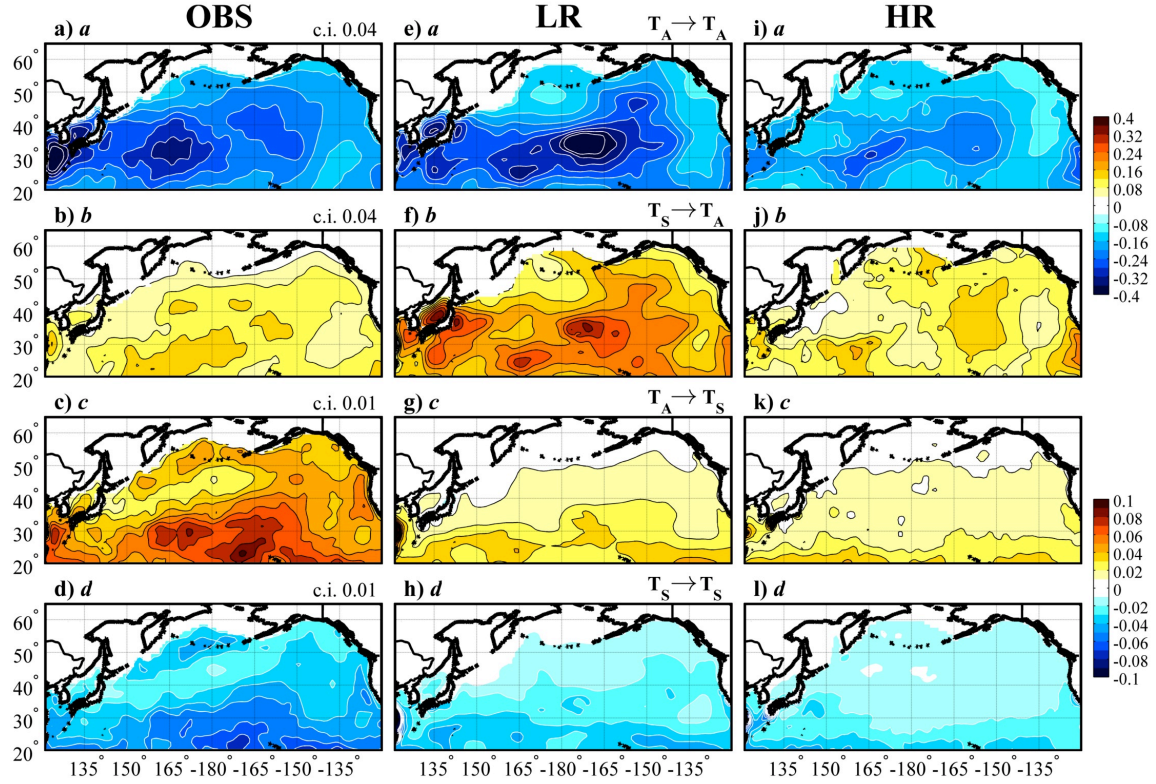


Figure 2: Spatial variability of the coefficients in the dynamical operator \mathbf{L} , found separately for every grid point using (a-d) OAFlux observations and (e-h) LR and (i-l) HR model output. See Section 3c for the details of the model configurations. The top (bottom) colorbar corresponds to the top (bottom) two rows. Coefficients a, d represent damping timescales (days^{-1}) of T_A (T_S), while coefficients b, c represent coupling strength ($b: T_S \rightarrow T_A$ and $c: T_A \rightarrow T_S$).

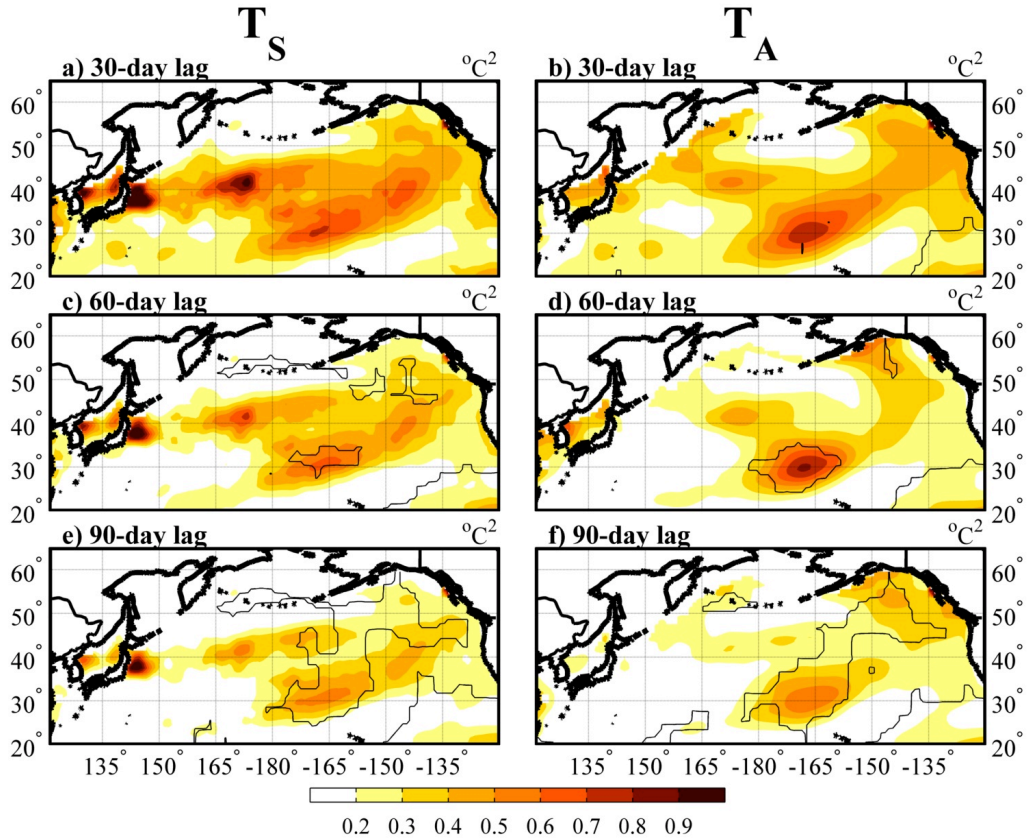


Figure 3: The observed (shading) lag-covariance for T_S (a,c,e) and T_A (b,d,f) when τ equals (a,b) 30 days, (c,d) 60 days, (e,f) 90 days. The contour encloses areas where the difference between the observed lag covariance and that predicted by the local-LIM exceeds the $p=0.025$ confidence level from a Monte Carlo test. Note that the local-LIM generally underestimates lagged covariance.

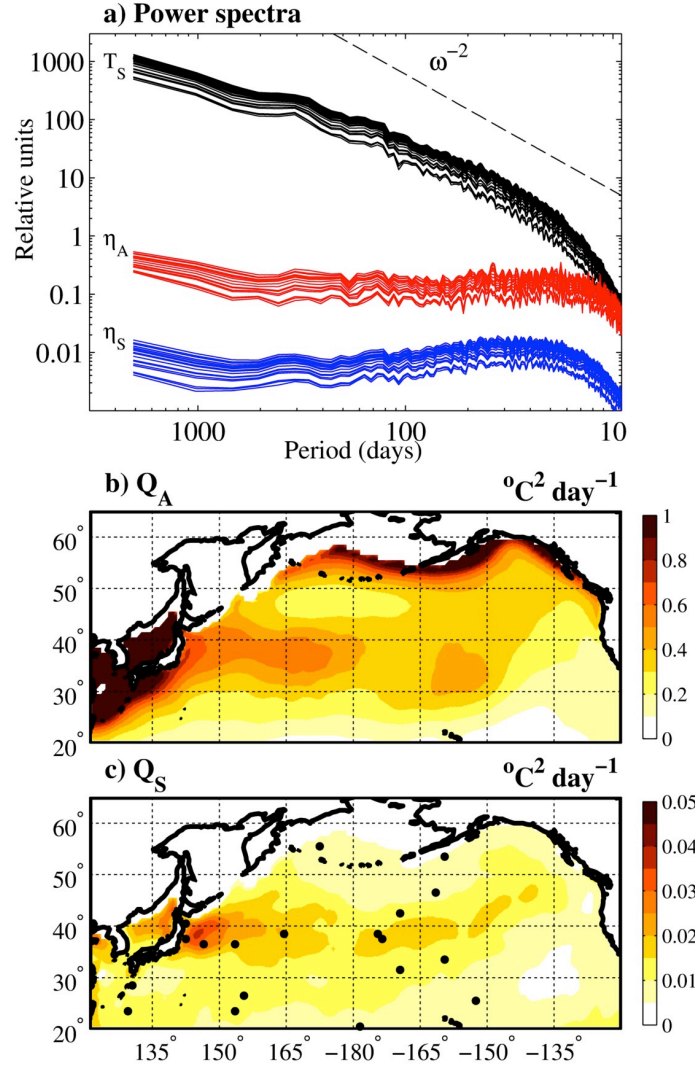


Figure 4: (a) The normalized power spectra of T_S (black), η_A (red), and η_S (blue) for 20 randomly sampled points, shown as black dots in (c) over the North Pacific. Note that η is determined using a finite differencing approximation shown in (6). The ω^{-2} line is shown to reference an undamped Markov model. For clarity, η_A (η_S) has been scaled by 0.03 (0.003). Thus, the values on the y-axis are only relative and should be used to note the ω -dependence of each spectrum. The noise covariance (\mathbf{Q}) of (b) T_A and (c) T_S calculated through (A3) separately at every grid point using \mathbf{L} and the observed covariance structure.

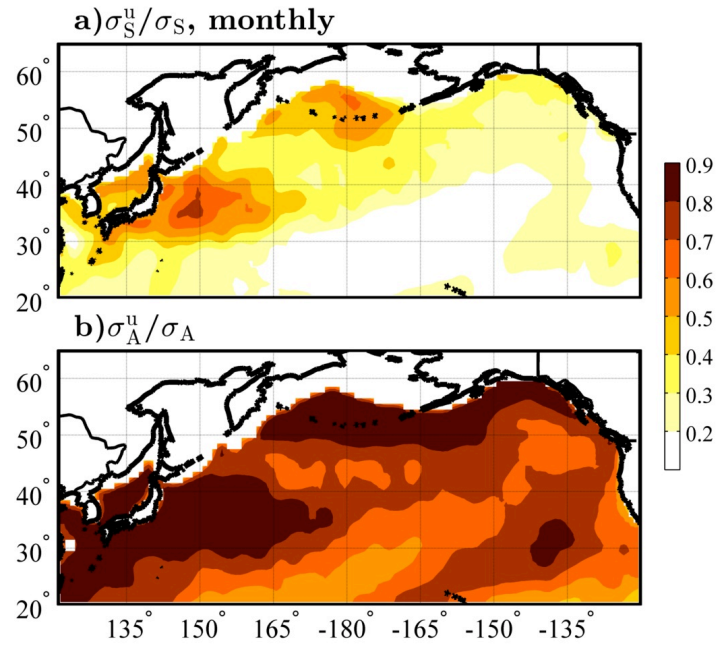


Figure 5: The fractional amount of retained (a) monthly averaged T_S and (b) total T_A variability after integrating (2) with the uncoupled operator \mathbf{L}^u and noise \mathbf{Q}^u .

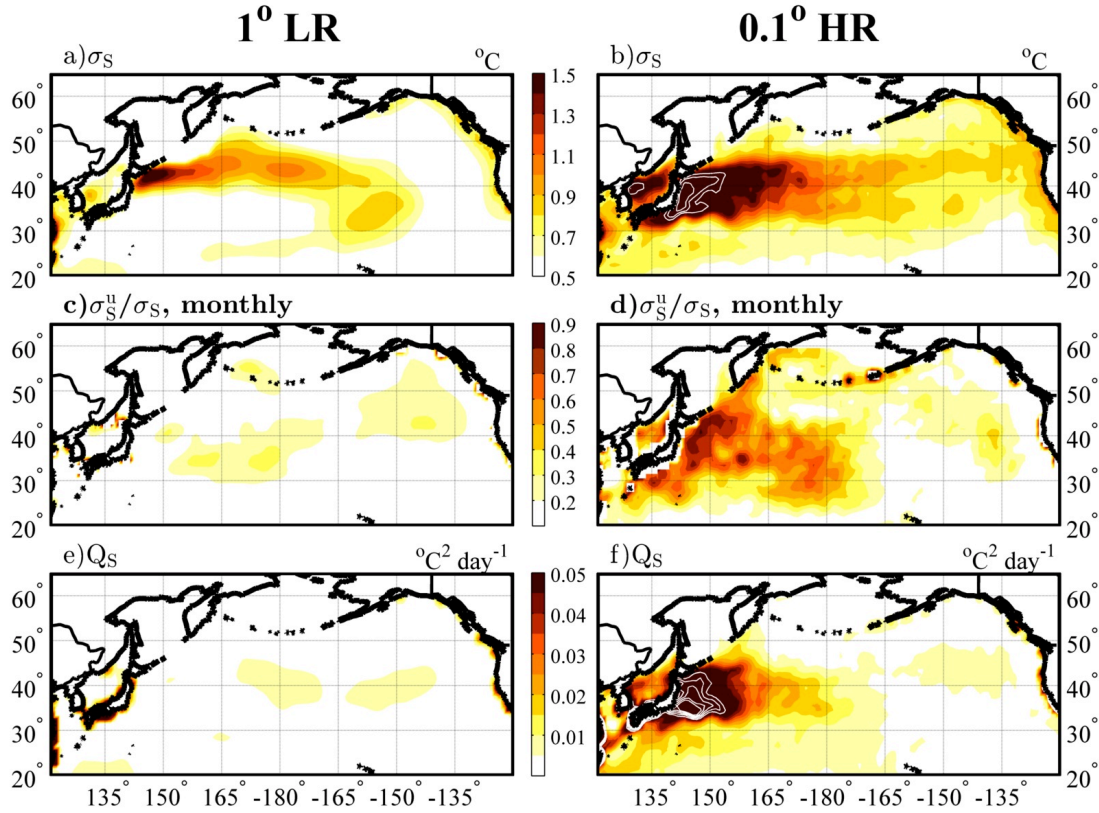


Figure 6: (a & b) Standard deviation of weekly averaged, extended winter (NDJFM) T_s anomalies from CCSM3.5 with an ocean model resolution of (a) 1° (LR) and (b) 0.1° (HR). These can be directly compared to Fig 1a. The white contours in (b) denote values exceeding the colorbar with a 0.2°C increment. (c & d) Same as Fig. 5a except for (c) LR and (d) HR. (e & f) Same as Fig. 4b except for (e) LR and (f) HR. The white contours in (f) denote values exceeding the colorbar with a 0.02°C² day⁻¹ increment.

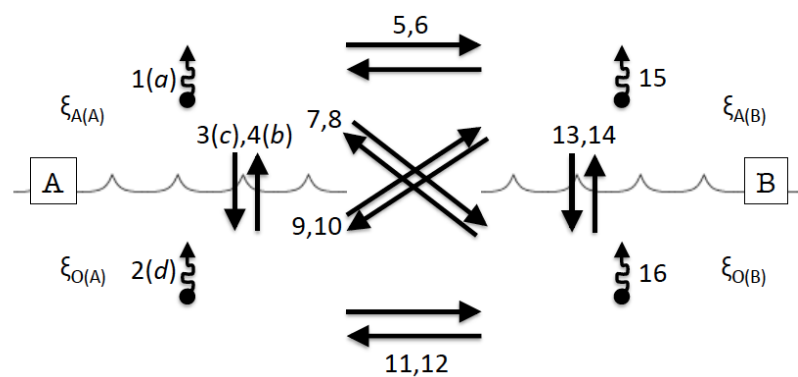


Figure 7: Schematic of interactions in a hypothetical T_A , T_S coupled model of two boxes, A and B. Processes are arbitrarily labeled for use within the discussion.

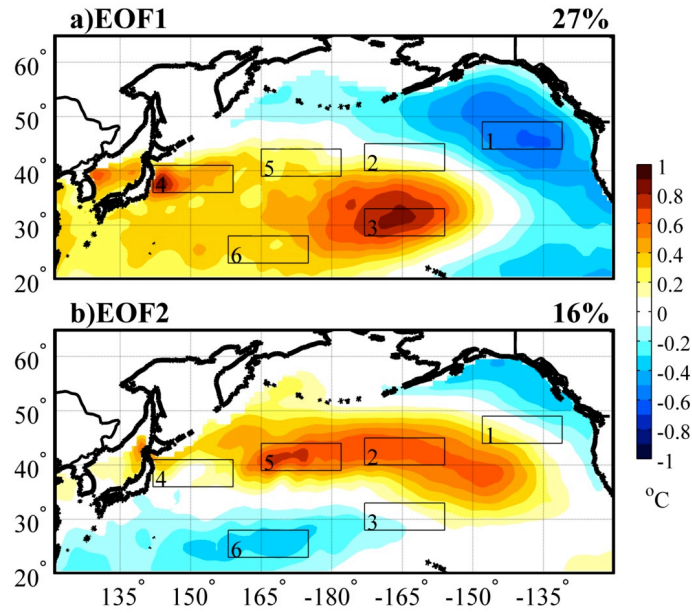


Figure 8: The leading two EOFs of weekly averaged, wintertime (NDJFM) SST anomalies over the North Pacific (20-60°N, 120°E-120°W). Boxes indicate the averaging regions used to build the box-LIM (see text). Values in the top right show the percent of variance explained by the EOF. Note that only these two EOFs are statistically separable using the technique of North et al. (1982).

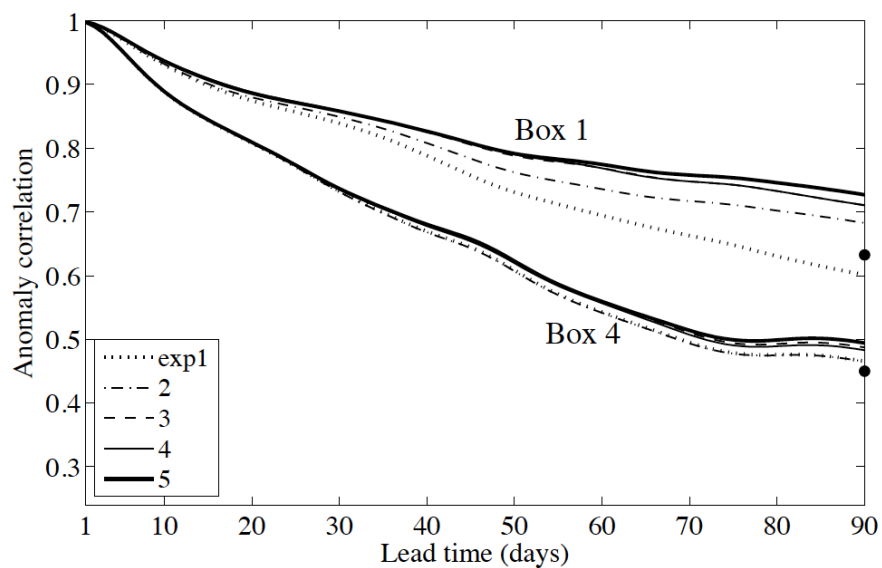


Figure 9: (a) Cross-validated skill as a function of lead-time for Box 1 and Box 4 T_s (anomaly correlation with observations) using **B** from the five experiments shown in Table 1. The black dots indicate the day 90 skill of Box 1 and 4 in the local-LIM. For Box 1, the dashed line showing the skill of exp3 is masked by the solid line showing exp4.

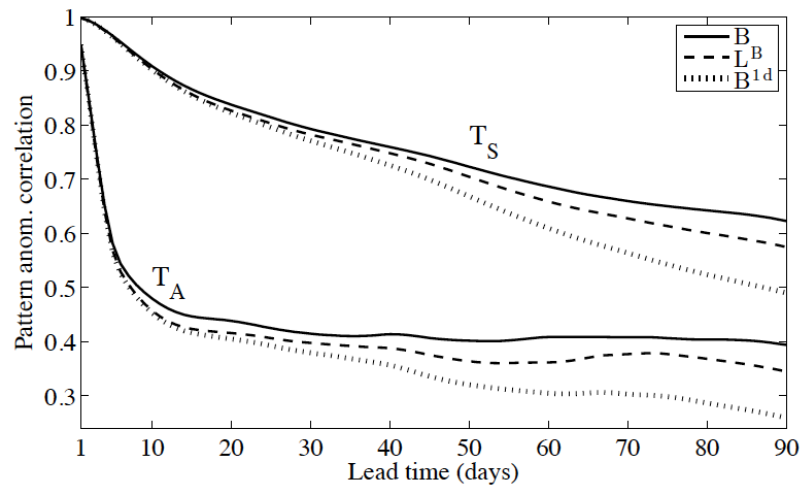


Figure 10: Cross-validated pattern anomaly correlation with observations of T_S and T_A using \mathbf{B} (solid), $\mathbf{L}^{\mathbf{B}}$ (dash) and \mathbf{B}^{1d} (dotted) from Exp3.

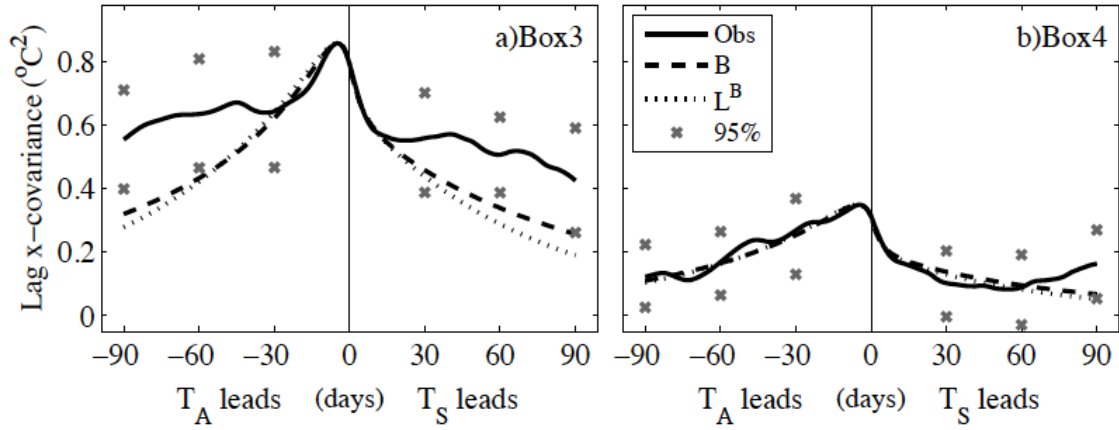


Figure 11: Observed (solid), and predicted (dash: using \mathbf{B} from exp3; dotted: using \mathbf{L}^B) lag cross-covariance between T_S and T_A as a function of lag time for (a) box 3 (east-central Pacific), and (b) box 4 (WBC region). T_A leads (lags) T_S when the lag time is negative (positive). Gray crosses indicate the upper (97.5%) and lower (2.5%) ranges using 200 iterations of a Monte Carlo test.

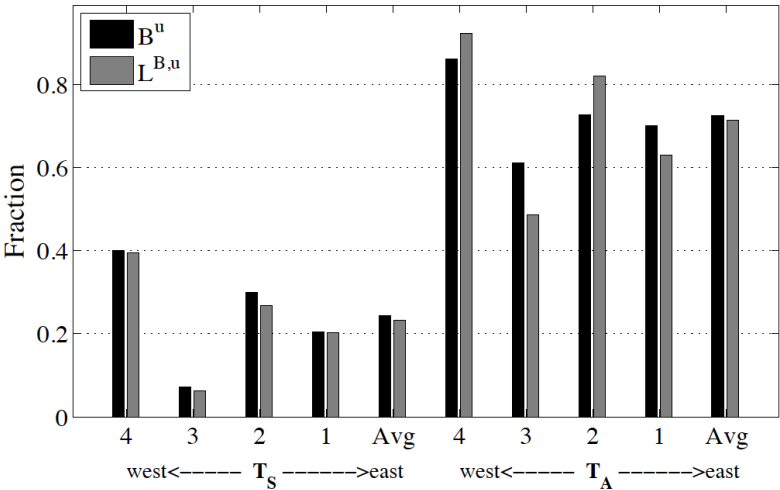


Figure 12: (Bottom) The fraction of T_S and T_A variance retained after uncoupling \mathbf{B} (from Exp3, black) and \mathbf{L}_B (gray) at every box. Also shown is the average across all boxes for T_S and T_A .